

physica **p** status **s** solidi **S**

www.pss-journals.com

reprint



Development of epitaxial $\text{Al}_x\text{Sc}_{1-x}\text{N}$ for artificially structured metal/semiconductor superlattice metamaterials

Editor's Choice

Bivas Saha^{1,2}, Sammy Saber^{1,2}, Gururaj V. Naik^{2,3}, Alexandra Boltasseva^{2,3}, Eric A. Stach^{1,4}, Eric P. Kvam^{1,2}, and Timothy D. Sands^{1,2,3}

¹ School of Materials Engineering, Purdue University, West Lafayette, IN-47907, USA

² Birck Nanotechnology Center, Purdue University, West Lafayette, IN-47907, USA

³ School of Electrical and Computer Engineering, Purdue University, West Lafayette, IN-47907, USA

⁴ Center for Functional Nanomaterials, Brookhaven National Laboratory, Upton, NY 11973-5000, USA

Received 19 June 2014, accepted 27 August 2014

Published online 23 September 2014

Keywords bandgap bowing, epitaxy, metal/semiconductor superlattices, rocksalt semiconductors

* Corresponding author: e-mail bsaha@purdue.edu, Phone: 765-413-4478, Fax: 765-494-7474

Epitaxial nitride rocksalt metal/semiconductor superlattices are emerging as a novel class of artificially structured materials that have generated significant interest in recent years for their potential application in plasmonic and thermoelectric devices. Though most nitride metals are rocksalt, nitride semiconductors in general have hexagonal crystal structure. We report rocksalt aluminum scandium nitride ($\text{Al}_x\text{Sc}_{1-x}\text{N}$) alloys as the semiconducting component in epitaxial rocksalt metal/semiconductor superlattices. The $\text{Al}_x\text{Sc}_{1-x}\text{N}$ alloys when deposited directly on MgO substrates are stabilized in a homogeneous rocksalt (single) phase

when $x < 0.51$. Employing 20 nm TiN as a seed layer on MgO substrates, the homogeneity range for stabilizing the rocksalt phase has been extended to $x < 0.82$ for a 120 nm film. The rocksalt $\text{Al}_x\text{Sc}_{1-x}\text{N}$ alloys show moderate direct bandgap bowing with a bowing parameter, $B = 1.41 \pm 0.19$ eV. The direct bandgap of metastable rocksalt-AlN is extrapolated to be 4.70 ± 0.20 eV. The tunable lattice parameter, bandgap, dielectric permittivity, and electronic properties of rocksalt $\text{Al}_x\text{Sc}_{1-x}\text{N}$ alloys enable high quality epitaxial rocksalt metal/ $\text{Al}_x\text{Sc}_{1-x}\text{N}$ superlattices with a wide range of accessible metamaterials properties.

© 2014 WILEY-VCH Verlag GmbH & Co. KGaA, Weinheim

1 Introduction Group III-metal nitride pseudobinary alloys are attractive for their potential applications in bandgap engineering for optoelectronic devices [1, 2], corrosion resistant hard coatings [3, 4], and as a component in metal/dielectric superlattices that are currently under investigation as metamaterials for thermionic and plasmonic devices [5–8]. Although comprehensive bulk data are lacking, studies of thin films indicate that ($\text{Al}_x\text{Sc}_{1-x}\text{N}$) exists as an equilibrium phase at standard temperature and pressure with the rocksalt crystal structure for compositions rich in ScN. For compositions close to AlN, the stable phase adopts the wurtzite crystal structure. A two-phase region separates these two single-phase regions of the pseudobinary diagram. In thin-film form, $\text{Al}_x\text{Sc}_{1-x}\text{N}$ is particularly attractive as a potential functional material, as it allows bandgap engineering in nitride semiconductors starting from

the infrared part of the spectrum (the indirect minimum gap of ScN is 0.9 eV [9]) to the deep UV-region (the minimum direct gap of AlN is 6.20 eV). The wurtzite phase of $\text{Al}_x\text{Sc}_{1-x}\text{N}$ has higher piezoelectric coefficients than any other nitride semiconductor [10, 11]. Although there are several reports [12, 13] of the physical properties of wurtzite- $\text{Al}_x\text{Sc}_{1-x}\text{N}$, not much attention has been given to the rocksalt phase. The only conclusion that we have drawn about its rocksalt phase from limited reports [10, 14] is that as x exceeds 0.5–0.6, the deposited film exhibits a measurable volume of the wurtzite phase. In this letter, we have stabilized rocksalt- $\text{Al}_x\text{Sc}_{1-x}\text{N}$ having a much higher aluminum nitride mole fraction ($\sim 82\%$) using an epitaxial stabilization technique with TiN as a stabilizing buffer layer. We report on optical properties including the direct energy gap and complex dielectric permittivity across the

composition range. The critical thickness for the nucleation of the wurtzite phase in these epitaxially stabilized $\text{Al}_x\text{Sc}_{1-x}\text{N}$ films is also evaluated. Our analysis has established that rocksalt- $\text{Al}_x\text{Sc}_{1-x}\text{N}$ has a tunable lattice constant, direct energy gap, dielectric permittivity, and electronic properties, which will allow growth of high quality epitaxial rocksalt metal/ $\text{Al}_x\text{Sc}_{1-x}\text{N}$ superlattice metamaterials [15, 16] having tunable properties that are potentially useful for optical devices, nanoelectronics, energy harvesting, thermal management systems, and hard coating tool applications.

Although there are many choices for metallic rocksalt phases with carrier concentrations characteristic of good metals (e.g., TiN, HfN, and ZrN), the range of suitable semiconducting phases that can be grown as a lattice-matched or pseudomorphic layer in a metal/semiconductor

superlattice has been limited to ScN [17]. ScN, however, cannot be lattice matched to TiN, and its applications are limited due to the lack of tunability of its properties. Most commonly known semiconductors such as the III-arsenides [18] (GaAs, InAs) or III-phosphides [18] crystallize in zincblende crystal structures. Many important II–VI semiconductors [18] also have the same zincblende crystal structure. When it comes to nitrides [18], GaN, InN, and AlN adopt hexagonal (wurtzite) structures. It is only the transition metal III-nitride semiconductors [19], such as ScN, YN, or LaN, that adopt the rocksalt crystal structure. While YN and LaN oxidize readily at room temperature, the challenges with ScN are that it has a small indirect gap of 0.9 eV [9], and usually has a high carrier concentration of 10^{20} – 10^{21} cm^{-3} arising primarily from impurities [19, 20]. Thus, solid-solution alloys of ScN with other nitride semiconductors [14, 21] could potentially offer the possibility of growing rocksalt nitride semiconductors that have tunable electronic and optical properties.

Since scandium (Sc) is isovalent with group III-metals, solid-solution alloys of ScN with another III-nitride semiconductor, AlN, could offer a tunable range of rocksalt semiconductor compositions. Recently, Akiyama et al. [10] have deposited textured $\text{Al}_x\text{Sc}_{1-x}\text{N}$ thin-film alloys with $0.54 < x < 1$ onto Si(001) substrates using rf-dual magnetron sputtering, and their results suggest that the films are wurtzite structured for $x > 0.59$, cubic for $x < 0.54$, and have a mixed phase microstructure in the intermediate range. Their analysis also established that the piezoelectric coefficient of wurtzite $\text{Al}_x\text{Sc}_{1-x}\text{N}$ films is up to four times larger than that of AlN, a result that has been subsequently verified by other groups [22]. Aside from some additional reports focused on wurtzite $\text{Al}_x\text{Sc}_{1-x}\text{N}$, rocksalt- $\text{Al}_x\text{Sc}_{1-x}\text{N}$ remains mostly unexplored in terms of its structural details, phase stability, optical properties, and electronic properties. Höglund et al. [14] deposited epitaxial $\text{Al}_x\text{Sc}_{1-x}\text{N}$ thin films using reactive magnetron sputtering and studied the effect of volume mismatch and electronic structure on its decomposition at higher temperatures. However, there has been no attempt to understand the solid-solution aluminum nitride solubility limit in $\text{Al}_x\text{Sc}_{1-x}\text{N}$ for the stable rocksalt phase. In this letter, we explore the homogeneity range of rocksalt- $\text{Al}_x\text{Sc}_{1-x}\text{N}$ in greater detail to provide the foundation for development of this material as a rocksalt semiconductor for optical and electronic applications.

2 Experimental section

2.1 Growth

(Al,Sc)N thin films were grown using reactive dc magnetron sputtering in a load-locked turbo-molecular pumped high vacuum deposition system with a base pressure of 10^{-8} Torr (PVD Products, Inc.). The growth chamber had the capability to accommodate four targets and was equipped with three dc power supplies. The Sc (99.998% purity), Al (99.99%), and Ti (99.99%) targets had dimensions of 2 in. diameter and 0.25 in. thickness. All depositions were performed with an Ar/N₂ mixture with the flow rates of Ar and N₂ being 4 and 6 sccm, which resulted in



Bivas Saha is a postdoctoral scholar at the Materials Science and Engineering Department of University of California, Berkeley, as well as an affiliate at the Materials Science Division of Lawrence Berkeley National Laboratory. He graduated with a Ph.D. degree from the Materials Engineering Department and the Birk Nanotechnology Center of

Purdue University in 2014. His research interests span from materials science to applied physics; specializing in thin film epitaxial growth, superlattices, and metamaterials designed to develop efficient thermoelectric, plasmonic and NEMs device elements. Dr. Saha is the recipient of Purdue University College of Engineering's Outstanding Graduate Student Research Award for Materials Engineering in 2014. He is a member of MRS, APS and has served as a graduate ambassador of the Birk Nanotechnology Center (2011–2012) and Discovery Park (2012–2013) at Purdue University.



Timothy D. Sands is a professor of electrical and computer engineering and materials science and engineering at Virginia Tech, where he also serves as its 16th president. Prior to joining Virginia Tech in 2014, Dr. Sands held positions at Purdue University (2002–2014), the University of California, Berkeley (1993–2002) and Bell Communications Research (Bellcore)

(1984–1993). Dr. Sands has published more than 250 refereed papers and conference proceedings and has been granted 19 patents in electronic and optoelectronic materials and devices. He is a fellow of IEEE and MRS, and a charter fellow of the National Academy of Inventors (NAI).

a sputter gas pressure of 5 mTorr. The targets were sputtered in constant power mode, and while the Al target was fixed at 200 W, the Sc target power was varied to achieve the desired ScN concentration in the $\text{Al}_x\text{Sc}_{1-x}\text{N}$ films. The substrates were maintained at 750 °C during deposition, as determined using an infrared pyrometer operated in the wavelength range of 0.8–1.1 μm , together with a thermocouple.

2.2 X-ray diffraction X-ray diffraction (symmetric 2θ - ω diffraction spectra) studies on the thin films were performed using Cu-K α 1 radiation in a PANalytical X'pert diffractometer. The diffractometer was equipped with triple-bounce monochromator to remove any contribution from Cu-K α 2.

2.3 HRTEM and MAADF-STEM An FEI Titan 80–300 scanning transmission electron microscope was used to study the microstructural aspects of the films. Cross-sectional samples for TEM study were prepared by the focused ion beam (FIB) *in situ* lift-out technique using an FEI Nova 200 dual beam scanning electron microscopy/FIB equipped with a Klocke nanomanipulator.

2.4 UV–visible spectroscopy A Lambda 950 UV–Vis–NIR spectrometer (PerkinElmer) with an integrating sphere was used to measure the reflection and transmission of the $\text{Al}_x\text{Sc}_{1-x}\text{N}$ films having $0 \leq x \leq 0.62$. The spectroscopic data were collected with a wavelength step of 10 nm. Since the MgO substrate does not absorb in the spectral region of our interest, all of these measurements were performed on samples grown on single-side polished MgO substrates.

2.5 Ellipsometry The optical properties of the superlattices were measured by spectroscopic ellipsometry (J. A. Woollam Co.). The ψ and δ plots were obtained for three different incidence angles, 30°, 50° and 70°, respectively at the spectral range of 320–2,000 nm with an interval of 10 nm. The ellipsometry data were fitted with a Drude model for TiN and a Drude–Lorentz model for the (Al,Sc)N layers.

3 Results and discussion

3.1 Structural characterization DC-magnetron sputtering was employed to deposit these materials, and the compositional analyses were performed by Rutherford backscattering spectrometry. The details of the growth technique and compositional analysis are presented in the methods and supplementary information (SI) sections respectively. A PANalytical X'pert Pro Diffractometer with a hybrid X-ray mirror and two-crystal monochromator that yields Cu-K α radiation ($\lambda = 1.54059 \text{ \AA}$) was used to study the diffraction patterns from $\text{Al}_x\text{Sc}_{1-x}\text{N}$ alloy films. The films were approximately 80 nm thick and grew with 002 orientation on (001) MgO substrates with the main film peak located at $2\theta = 39$ – 42° (Fig. 1a). Four equally spaced asymmetric φ -peaks (not shown here) indicate their epitaxial nature. The 002 diffraction peak shifts to the high angle side

as aluminum nitride is added to the ScN matrix, suggesting a decrease in the out-of-plane lattice constant (c) as x increases from 0 to 0.62. Although AlN in its stable form has the hexagonal (wurtzite) crystal structure, it also has a high pressure rocksalt (cubic) phase [23] with a lattice constant of 4.08 \AA ; as a result, the lattice constant of rocksalt $\text{Al}_x\text{Sc}_{1-x}\text{N}$ with $0 \leq x \leq 0.62$ decreases with increasing AlN mole fraction. The diffraction spectra also show that the 002 peak completely disappears when $x = 0.72$, which is indicative of the complete transition from a rocksalt- $\text{Al}_x\text{Sc}_{1-x}\text{N}$ film to a stable wurtzite- $\text{Al}_x\text{Sc}_{1-x}\text{N}$ film. The aluminum nitride mole fraction for this cubic to wurtzite phase transition in $\text{Al}_x\text{Sc}_{1-x}\text{N}$ in our case is higher than that reported by Akiyama et al. [10] possibly due to differences in substrates. We have grown these films on (001) MgO which allows epitaxial growth, whereas Akiyama et al. grew their films on (100) Si resulting in polycrystalline films. Careful observation of Fig. 1a also indicates that the peak height of the 002 diffraction peak is smaller for $x = 0.62$ in comparison with $x = 0.51$, and a 0002 wurtzite- $\text{Al}_x\text{Sc}_{1-x}\text{N}$ peak appears at $2\theta \sim 36.6^\circ$. Since all of the X-ray scans were performed under identical conditions and all of these films had similar thickness, this suggests that films with $x = 0.62$ exhibit a two-phase microstructure and become entirely wurtzite at $x = 0.72$. The out-of-plane lattice constant (c) follows a linear relationship ($c = 4.55 - 0.36x$) with Al mole fraction in the rocksalt phase range $0 \leq x \leq 0.62$. The in-plane lattice constant (a) determined from the asymmetric 222 peak also shows a linear trend ($a = 4.49 - 0.37x$) (presented in the SI). The (c/a) ratios of all the films have similar values close to 1.00 suggesting that the films are partially to fully strain relaxed. The full width at half maximum (FWHM) of the ω -scan (see inset of Fig. 1a) is representative of the crystal quality of the alloy films and decreases with increasing AlN concentrations (except for the $x = 0.13$ case). Since the in-plane lattice constant of films decreases with increasing aluminum nitride content, the lattice mismatch between the films and substrate (MgO with lattice constant $a = 4.21 \text{ \AA}$) decreases, thus favoring better lattice matching between the films and the substrate, which allows high quality crystal growth as evidenced by smaller values of the FWHM.

To stabilize rocksalt $\text{Al}_x\text{Sc}_{1-x}\text{N}$ with AlN mole fractions above ~ 0.62 , we use epitaxial stabilization [24] with a 20 nm TiN buffer layer on top of the MgO substrate, followed by the $\text{Al}_x\text{Sc}_{1-x}\text{N}$ alloy film, and then a cap layer of 20 nm TiN. The X-ray diffraction spectra (see Fig. 1b) of the $\text{Al}_{0.72}\text{Sc}_{0.28}\text{N}$, $\text{Al}_{0.82}\text{Sc}_{0.18}\text{N}$, and $\text{Al}_{0.88}\text{Sc}_{0.12}\text{N}$ alloy films, having thicknesses of 135, 120, 120 nm, respectively, and sandwiched between 20 nm TiN layers on top and bottom suggest that the first two alloy films are epitaxial and cubic with the main 002 diffraction peak close to the 002 MgO peak, while the $\text{Al}_{0.88}\text{Sc}_{0.12}\text{N}$ alloy film is composed of polycrystalline wurtzite material. Note that the main 002 diffraction peak in the spectrum from the $\text{Al}_{0.72}\text{Sc}_{0.28}\text{N}$ splits into two peaks, one at 42.26° corresponding to an out-of-plane lattice constant of 4.27 \AA of $\text{Al}_{0.72}\text{Sc}_{0.28}\text{N}$ and one at 42.48° corresponding to the lattice constant of TiN

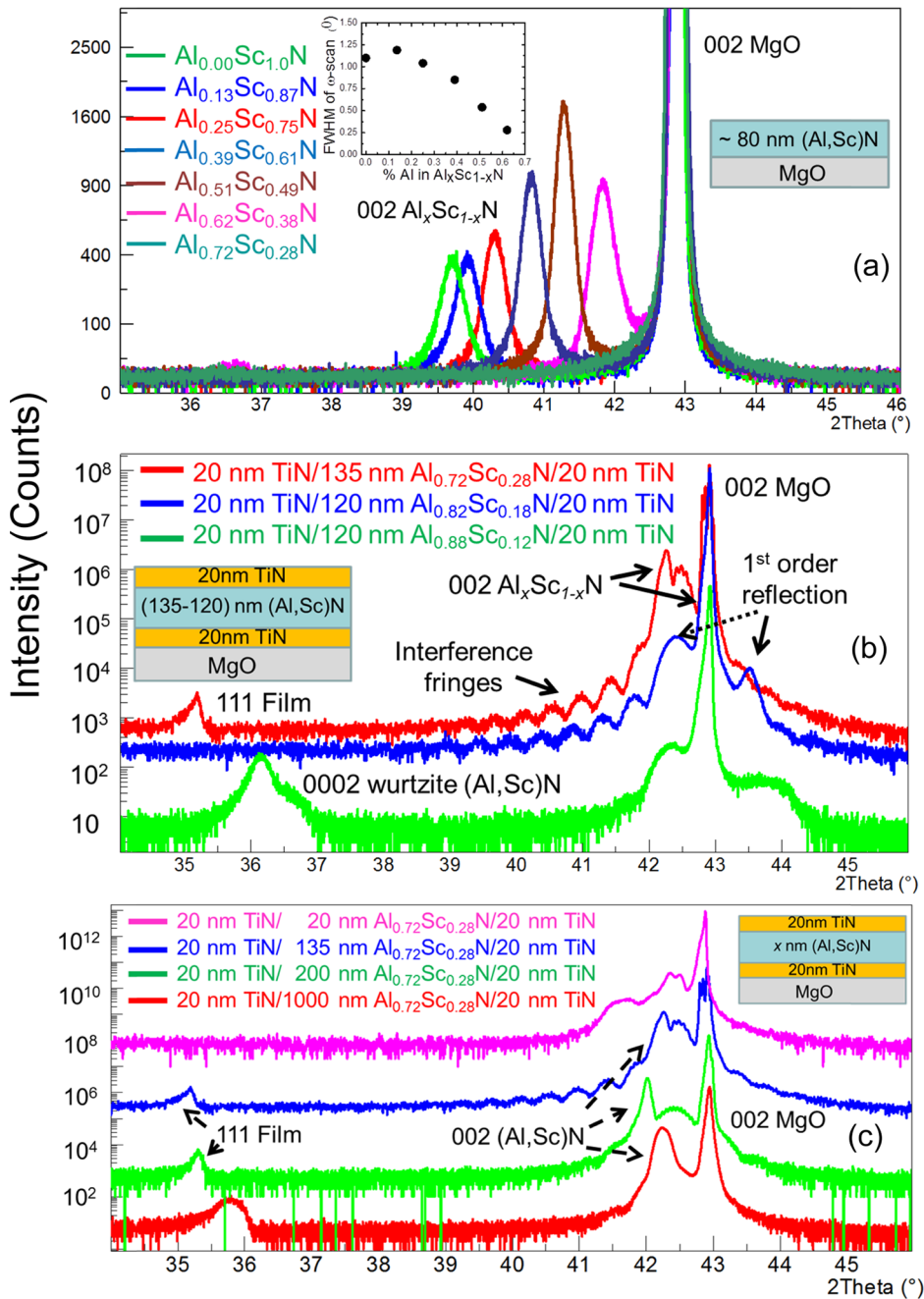


Figure 1 (a) XRD spectra of $\text{Al}_x\text{Sc}_{1-x}\text{N}$ films grown directly on MgO (001) substrates. For the $\text{Al}_{0.72}\text{Sc}_{0.28}\text{N}$ film, the 002 diffraction peak vanishes, suggesting a rocksalt-to-wurtzite transition at aluminum nitride mole fractions between $x = 0.51$ and 0.72 . The inset represents the full width at the half maximum of the rocking curves, which decreases with increasing aluminum nitride mole fraction beyond $x = 0.13$, suggestive of improving crystal quality. (b) Symmetric 2θ - ω diffraction spectra of $\text{Al}_x\text{Sc}_{1-x}\text{N}$ films sandwiched between 20 nm TiN layers. The 002 rocksalt $\text{Al}_x\text{Sc}_{1-x}\text{N}$ diffraction peaks are clearly visible, suggesting that the $\text{Al}_{0.72}\text{Sc}_{0.28}\text{N}$ and $\text{Al}_{0.82}\text{Sc}_{0.18}\text{N}$ are epitaxially stabilized in the rocksalt phase, while the $\text{Al}_{0.88}\text{Sc}_{0.12}\text{N}$ film is polycrystalline and wurtzite. (c) Diffraction spectra of $\text{Al}_{0.72}\text{Sc}_{0.28}\text{N}$ films having different thicknesses and sandwiched between 20 nm TiN layers. It is worth noting that, even when the film thickness is as large as a micron, the $\text{Al}_{0.72}\text{Sc}_{0.28}\text{N}$ films still show cubic diffraction patterns.

($c = 4.25 \text{ \AA}$). Satellite reflections arising due to interference of X-rays scattered from internal interfaces are also clearly observed, which suggests sharp TiN/ $\text{Al}_{0.72}\text{Sc}_{0.28}\text{N}$ interfaces. The main 002 diffraction peak of $\text{Al}_{0.82}\text{Sc}_{0.18}\text{N}$ is

buried under the MgO substrate peak and only the two first-order interference fringes are observed in the XRD spectrum. We also see clear interference fringes and the absence of the 0002 wurtzite peak in the spectrum from $\text{Al}_{0.82}\text{Sc}_{0.18}\text{N}$,

indicating that this film is cubic rocksalt. Apart from the main 002 peak in the spectra of the first two alloy films, we also see some minor cubic 111 peaks at $2\theta = 35.2^\circ$ that sporadically appear in these films.

In summary, the epitaxial stabilization technique allowed us to grow rocksalt $\text{Al}_x\text{Sc}_{1-x}\text{N}$ with $0.62 \leq x \leq 0.82$, which would otherwise exhibit the wurtzite crystal structure when grown directly on MgO substrates. In other words, the TiN underlayer has increased the AlN mole fraction (x) in $\text{Al}_x\text{Sc}_{1-x}\text{N}$ corresponding to the nucleation of the wurtzite phase during growth from a value in the range of 0.51–0.62 to 0.82–0.88 and the minimum mole fraction for growth of entirely wurtzite films from 0.62–0.72 to 0.82–0.88.

3.2 Microscopic characterization The 120 nm $\text{Al}_{0.72}\text{Sc}_{0.28}\text{N}$ alloy film sandwiched between 20 nm TiN layers was investigated with high-resolution transmission electron microscopy (HRTEM). The low magnification image Fig. 2a shows clear and sharp TiN/MgO and $\text{Al}_{0.72}\text{Sc}_{0.28}\text{N}$ /TiN interfaces on the substrate side; the upper TiN/ $\text{Al}_{0.72}\text{Sc}_{0.28}\text{N}$ interface appears to be rougher on a nanometer scale. Fast Fourier Transforms (FFT) from different parts of the images of the $\text{Al}_{0.72}\text{Sc}_{0.28}\text{N}$ alloy film confirm that it is cubic rocksalt throughout as indicated by the XRD analysis. Due to very good lattice matching between TiN (4.24 Å) and $\text{Al}_{0.72}\text{Sc}_{0.28}\text{N}$ (4.27 Å), we do not detect any misfit dislocations at the interface. The high magnification image of the bottom $\text{Al}_{0.72}\text{Sc}_{0.28}\text{N}$ /TiN interface (see Fig. 2b) shows the cube-on-cube epitaxial relationships of TiN(001)[100]||MgO(001)[100] and $\text{Al}_{0.72}\text{Sc}_{0.28}\text{N}$ (001)[100]||TiN(001)[100], also verified by XRD φ -scans (not shown here).

The 20 nm TiN seed layer helps in stabilizing the rocksalt phase in $\text{Al}_x\text{Sc}_{1-x}\text{N}$ films with $0.62 \leq x \leq 0.82$, which otherwise exhibit the wurtzite phase when grown

directly on 002 MgO substrates. We offer two contributing factors that may help to explain the stabilization of the rocksalt phase. First, by using TiN as seed layer, the lattice mismatch has been reduced from 1.4% (between $\text{Al}_{0.72}\text{Sc}_{0.28}\text{N}$ and MgO) to 0.4% (between $\text{Al}_{0.72}\text{Sc}_{0.28}\text{N}$ and TiN) if the TiN layer is completely relaxed. A second contributing factor may be the reduction in bond polarity mismatch with $\text{Al}_x\text{Sc}_{1-x}\text{N}$ and the underlying growth substrate (MgO or TiN/MgO). A rough estimate of the bond polarity (calculated by evaluating the electronegativity difference between the cation and anion) suggests that the nitride materials (TiN, AlN, and ScN) have significantly smaller bond polarities (1.5, 1.43, and 1.68, respectively) than MgO (2.13). Therefore, TiN offers a substrate that is effectively homoepitaxial, yielding a low excess interfacial free energy by virtue of both the close lattice match and the similar bond polarity.

3.3 Critical thickness of the metastable film

Having stabilized rocksalt $\text{Al}_x\text{Sc}_{1-x}\text{N}$ with high AlN mole fractions, we addressed the critical thickness for stabilizing the rocksalt phase of these alloys taking $\text{Al}_{0.72}\text{Sc}_{0.28}\text{N}$ as a model composition (see Fig. 1c). Preserving the TiN 20 nm seed layer and the top 20 nm TiN cap layer, the thickness of the $\text{Al}_{0.72}\text{Sc}_{0.28}\text{N}$ alloy was varied from 20 to 1,000 nm. For the 20 nm $\text{Al}_{0.72}\text{Sc}_{0.28}\text{N}$ film, the 002 peak is separated into two; one at $2\theta = 41.6^\circ$ corresponding approximately to the bulk value (obtained from the $c = 4.55 - 0.36x$ relationship) of the $\text{Al}_{0.72}\text{Sc}_{0.28}\text{N}$ alloy, and the other at $2\theta = 42.48^\circ$, corresponding to the lattice constant of TiN. The case for the 135 nm $\text{Al}_{0.72}\text{Sc}_{0.28}\text{N}$ alloy was already discussed in the last section. The interference fringes in the spectrum from the 135 nm $\text{Al}_{0.72}\text{Sc}_{0.28}\text{N}$ film disappear as the alloy film thickness is increased to 200 nm, but a strong 002 cubic peak corresponding to the lattice constant $c = 4.29$ Å remains, as well as a small 111 rocksalt peak at $2\theta = 35.1^\circ$. Thus, the

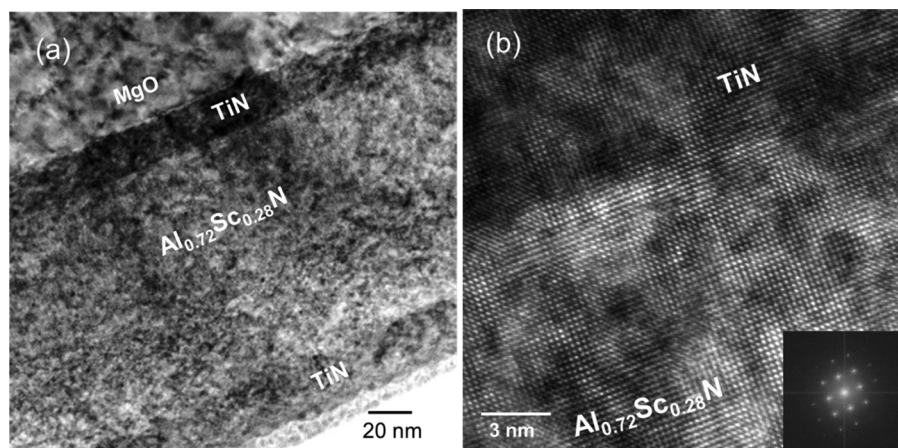


Figure 2 (a) Transmission electron microscope (TEM) image of the $\text{Al}_{0.72}\text{Sc}_{0.28}\text{N}$ film sandwiched between 20 nm TiN layers. Sharp and clear TiN/MgO and $\text{Al}_{0.72}\text{Sc}_{0.28}\text{N}$ /TiN interfaces are observed. (b) High-magnification transmission electron microscope (HRTEM) image of the TiN and $\text{Al}_{0.72}\text{Sc}_{0.28}\text{N}$ interface (substrate side) showing cube-on-cube epitaxial crystal growth. The inset shows FFT taken from the $\text{Al}_{0.72}\text{Sc}_{0.28}\text{N}$ region demonstrating a cubic diffraction pattern.

sandwiched $\text{Al}_{0.72}\text{Sc}_{0.28}\text{N}$ alloy film of 200 nm thickness is rocksalt. The case for the alloy film having a thickness of 1,000 nm is very interesting, as the XRD spectra suggests the presence of both the 002 cubic and 0002 wurtzite diffraction peaks, representing a mixed phase alloy film. The main 002 cubic peak corresponds to a c -axis lattice constant of 4.27 Å, consistent with the Al to Sc ratio, while the 0002 wurtzite peak is positioned slightly to the low angle side compared to the $\text{Al}_{0.88}\text{Sc}_{0.12}\text{N}$ case, corresponding to its larger c -axis lattice constant. However, the 002 cubic diffraction peak height is 1,000 times larger than the 0002 wurtzite peak, suggesting that the film is primarily cubic with some c -axis oriented wurtzite captured in XRD. Of course, symmetric XRD scans will not detect misoriented grains of the wurtzite phase, so these scans alone are not sufficient for accurately estimating volume fractions. Nevertheless, the above analysis indicate that metastable $\text{Al}_{0.72}\text{Sc}_{0.28}\text{N}$ grown with a TiN buffer layer exhibits a critical thickness in excess of 135 nm with respect to the nucleation of the wurtzite phase during deposition.

4 Optical properties We now focus on the optical properties of these alloy films. Reflectance and transmission spectra of the alloy films with $0 \leq x \leq 0.62$ were measured with a Perkin-Elmer 950 UV–visible spectrometer in the wavelength range 320–860 nm and subsequently used to calculate the absorption coefficient (α) (presented in Fig. 3b) and used in a Tauc plot ($(\alpha\hbar\omega)^2$ vs. $\hbar\omega$) as presented in Fig. 3c to extract the direct bandgap of the alloy films. For the $\text{Al}_x\text{Sc}_{1-x}\text{N}$ films having higher aluminum nitride content ($0.72 \leq x \leq 0.82$) and grown epitaxially in the rocksalt phase by sandwiching between 20 nm TiN layers, reflection and transmission from TiN hinders extraction of optical properties. Hence we employed spectroscopic ellipsometry in the wavelength range of 300–2,000 nm to extract the dielectric permittivity of the $\text{Al}_x\text{Sc}_{1-x}\text{N}$ alloy layers. Experimental details of both the ellipsometry measurement and the retrieval procedure are presented in Section 2.

The absorption coefficient (α) of ScN (presented in Fig. 3b) shows a steep increase at 2.25 eV corresponding to the direct bandgap, as previously reported by several research groups [19]. With the introduction of AlN in the ScN matrix, the peaks in the absorption coefficient (α) are blue-shifted, suggesting an increase in the direct bandgap of the alloy films. The nature of the absorption coefficient is quite similar for $\text{Al}_x\text{Sc}_{1-x}\text{N}$ alloys with $x = 0$ –0.51, as all of these films exhibit the rocksalt crystal structure. The nature of the absorption coefficient of $\text{Al}_{0.62}\text{Sc}_{0.38}\text{N}$, which has a mixed cubic-wurtzite microstructure, resembles that of an $\text{Al}_{0.72}\text{Sc}_{0.28}\text{N}$ film grown without the TiN stabilization layer that has been found by X-ray diffraction to be entirely wurtzite. The tail of the absorption coefficient below the direct bandgap for the $\text{Al}_{0.13}\text{Sc}_{0.87}\text{N}$ film has a slightly larger value compared to that of other films possibly due to presence of lattice-mismatch-related defects, which are manifested in higher values of FWHM of the ω -scan, as seen in the inset of Fig. 1a.

The direct bandgap values are extracted from the absorption coefficient data using two different techniques [25]. In the first case, $(\alpha\hbar\omega)^2$ is plotted as a function of the incident photon energy, where a steep increase in $(\alpha\hbar\omega)^2$ is associated with direct bandgap absorption (plotted as black dots in Fig. S2 of the Supporting Information). Under this technique, one assumes that the band edge of the semiconductor is parabolic (a reasonable approximation for most semiconductors). In the second case, an alternative procedure is adapted where it is assumed that the changes in the absorption coefficient are all due to variations in the direct energy gap, thereby neglecting any changes in absorption due to the sub-bandgap regions of the spectrum. Using this procedure, red circles (plotted in Fig. S2) are obtained by using the photon energy corresponding to the absorption coefficient $\alpha = 1 \times 10^5 \text{ cm}^{-1}$, which is the absorption coefficient of ScN at the energy corresponding to its direct gap (2.25 eV) as determined by the first procedure. Both techniques yield values that deviate from each other by less than 1%. For $\text{Al}_x\text{Sc}_{1-x}\text{N}$ films having $0.62 \leq x \leq 0.88$ and with TiN buffer and capping layers, ellipsometry-based extraction of the direct gap follows the extrapolated path of the stable rocksalt $\text{Al}_x\text{Sc}_{1-x}\text{N}$ (see Fig. 3a). The $\text{Al}_{0.88}\text{Sc}_{0.12}\text{N}$ film with the wurtzite crystal structure has a direct gap value of 4.2 eV, a value that is larger than the predicted linearly extrapolated value if the optical absorption properties were governed by the rocksalt phase.

Careful observations of the measured direct bandgap also suggest some degree of bowing. Bandgap bowing in ternary semiconductor alloys is a well-known phenomenon [26, 27] and has been observed in semiconductors such as (In,Ga)N, (Al,Ga)N, and Ga(As,N). We use a quadratic relationship $E_g^T(x) = x \cdot E_{\text{AlN}}^T + (1-x) \cdot E_{\text{ScN}}^T - B \cdot x \cdot (1-x)$ to extract the bowing parameter and the direct bandgap of rocksalt-AlN (since there is no experimental report on rocksalt-AlN's direct bandgap, and the limited number of DFT calculations have been inconclusive about the bandgap value). Our results suggest (see SI) that a moderate bowing parameter of 1.41 ± 0.19 eV fits the bandgap over the entire stable rocksalt compositional range ($x \leq 0.62$). This moderate bowing parameter of $\text{Al}_x\text{Sc}_{1-x}\text{N}$ alloys is very close to the values of (Al,Ga)N (1.0 eV) [26] and (In,Ga)N [27] (1.4–2.5 eV). The direct gap of rocksalt-AlN that we have extracted from the fitting is 4.70 ± 0.20 eV. Though obtained from an indirect procedure, this is the first experimental report of the direct bandgap of rocksalt-AlN, and the value agrees well with Camp et al.'s [28] calculation of 4.99 eV.

This direct gap absorption in ScN results from the electronic absorption from the Γ -point of the valence band maxima to the Γ -point of the conduction band minimum, as can be seen from an electronic structure calculation of ScN [9]. However our modeling results have also suggested that the conduction band minimum of ScN is located at the X point of the Brillouin zone, making ScN an indirect bandgap semiconductor with an indirect Γ –X gap of 0.9 eV. Recent DFT analyses [29, 30] have further established that rocksalt-AlN is also an indirect bandgap semiconductor

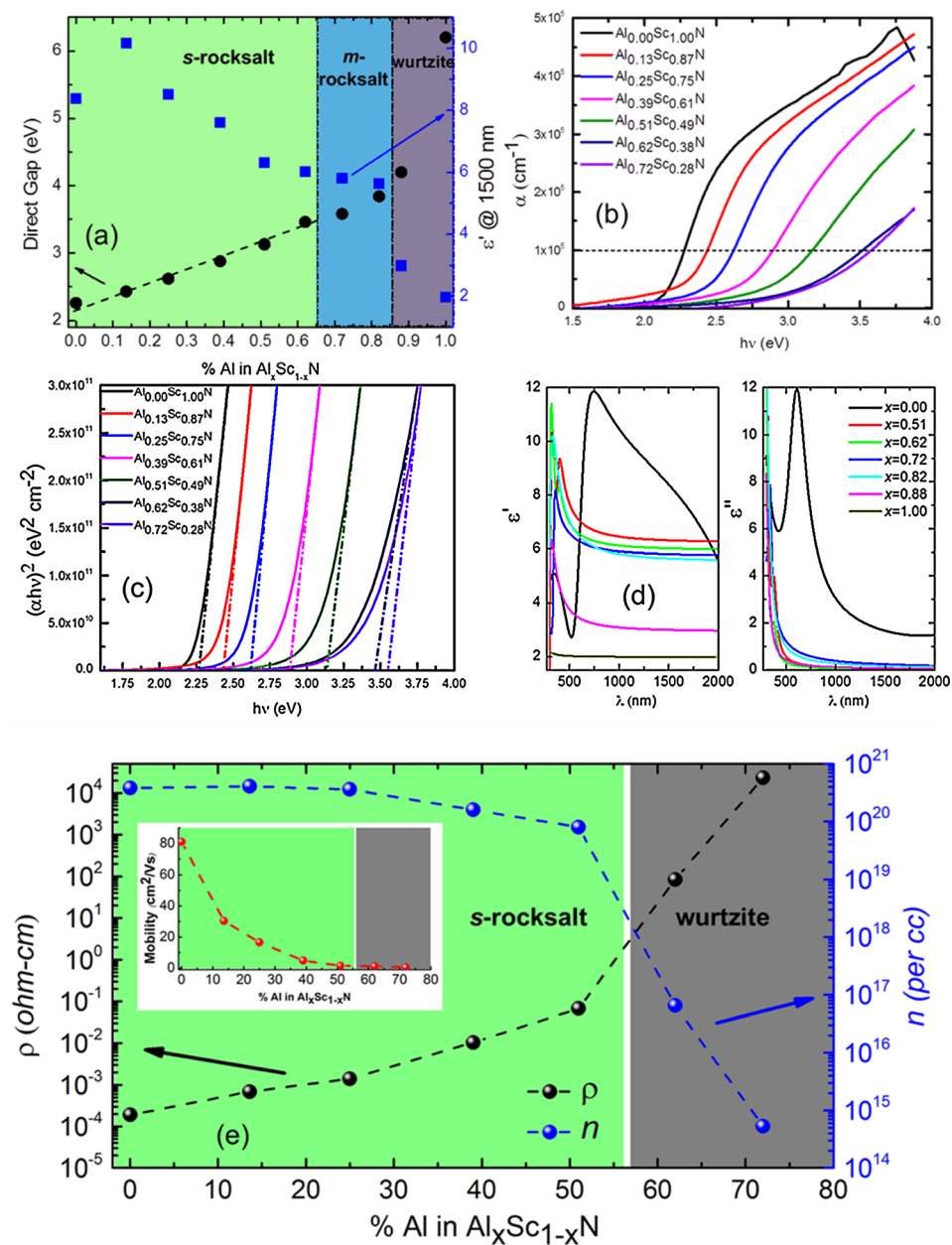


Figure 3 (a) Phase diagram of optical properties (direct energy bandgap and dielectric permittivity corresponding to near-infrared wavelength of 1.5 μm) as a function of aluminum nitride mole fraction in $\text{Al}_x\text{Sc}_{1-x}\text{N}$ films. Three different regions, that is, stable rocksalt phase (denoted as s-rocksalt), metastable rocksalt phase (denoted as m-rocksalt) and wurtzite phase are seen with their respective optical properties. The bandgap of pure AlN is adopted from Ref. [24]. (b) Absorption coefficient (α) of the rocksalt- $\text{Al}_x\text{Sc}_{1-x}\text{N}$ grown directly on MgO substrates. The horizontal line at $\alpha = 10^5 \text{ cm}^{-1}$ corresponds to the absorption coefficient of pure ScN at its direct bandgap. (c) Tauc plot ($(\alpha h\nu)^2$ vs. $h\nu$) plot of the films to extract the direct energy bandgap. (d) The real and imaginary part of the dielectric permittivity (ϵ' and ϵ'') of the stable rocksalt, metastable rocksalt, and wurtzite $\text{Al}_x\text{Sc}_{1-x}\text{N}$ films over the near UV–visible to near IR range of the optical spectra. For the sake of clarity, ϵ' and ϵ'' from two stable rocksalt $\text{Al}_x\text{Sc}_{1-x}\text{N}$ films having $x = 0.51$ and $x = 0.62$ are presented. (e) Room temperature electronic properties of the (Al,Sc)N thin film as a function of AlN concentration in ScN matrix. Resistivity increases dramatically due to a decrease in carrier concentration at the sample's transition from the rocksalt phase to the wurtzite phase.

with an indirect band gap of 4.2 eV. Since both of the parent materials of the alloy are indirect gap semiconductors, it is expected that the $\text{Al}_x\text{Sc}_{1-x}\text{N}$ films will also exhibit indirect gaps. However the indirect bandgap absorption of ScN

and $\text{Al}_x\text{Sc}_{1-x}\text{N}$ films is not obvious in experiments because the absorption cross-sections of indirect transitions are extremely small and an $\sim 80 \text{ nm}$ thick film does not yield sufficient absorption to extract the indirect gap. The nearly

linear variation of the direct gap as aluminum nitride is added in the ScN matrix is expected, as Al and Sc both are group-III elements, with Al higher in periodic table than Sc, and wurtzite AlN having a much larger bandgap of 6.2 eV.

For the potential application of rocksalt- $\text{Al}_x\text{Sc}_{1-x}\text{N}$ as a dielectric layer in optical metamaterials comprised of metal/ $\text{Al}_x\text{Sc}_{1-x}\text{N}$ superlattices and also for its use in any optoelectronic applications, it is important to know the dielectric permittivity of the alloy as a function of the aluminum nitride content over the entire visible to near IR spectral range. The real part of the permittivity (ϵ') is plotted in Fig. 3a as a function of x for a wavelength of 1,500 nm, an important wavelength for telecommunications. With an increase in x in the $\text{Al}_x\text{Sc}_{1-x}\text{N}$ films, the real part of the permittivity decreases except for the case of ScN, whose long wavelength real permittivity is lower than that of $\text{Al}_{0.13}\text{Sc}_{0.87}\text{N}$ for reasons explained below. Since the dielectric constant measures how strongly the electronic charge in the material can adjust to shield an external electric field, the smaller the bandgap of the semiconductor, the more effective the screening and the higher the dielectric constant. As the bandgap increases, the electric field cannot mix the electronic states in the valence band with the electronic states in the conduction band, so that the electrons polarize less, which makes the permittivity smaller. Hence, we see that the films having high aluminum nitride content have lower dielectric permittivity. Figure 3a also suggests a discontinuous drop of the permittivity near $x = 0.82$ when the ϵ' value changes from 5.64 to 2.99 indicative of the rocksalt-to-wurtzite $\text{Al}_x\text{Sc}_{1-x}\text{N}$ transition.

Figure 3d, showing the real and imaginary part of the permittivity as a function of the wavelength, gives us detailed information about the nature of the individual films. For pure ScN, a Lorentz oscillator captures the direct energy gap in the 660–780 nm spectral regions, while the high wavelength range is dominated by free-carrier Drude absorption that decreases the overall permittivity. ScN films grown with the sputtering technique have a carrier concentration of $2\text{--}5 \times 10^{20} \text{ cm}^{-3}$ arising primarily from oxygen impurities and nitrogen vacancies. The strength of the free carrier Drude absorption is very high, as also shown in our previous studies [19]. The peak value of ϵ' at the position of the interband transition is 11.9, consistent with our previous theoretical and experimental analysis [9, 19] and is comparable with Si, which has an indirect gap of 1.1 eV and a real part of the permittivity $\epsilon' = 11.7$. As aluminum nitride is added in the ScN matrix, the carrier concentration of the film decreases, which weakens the strength of the free carrier Drude absorption, manifested as a nearly constant value of the permittivity over the near-IR spectral region. The peak of the Lorentz oscillator also shifts to the near-UV region to capture the direct energy gaps (see Fig. 3a). Our observation of a smaller ϵ' at $\lambda = 1,500 \text{ nm}$ for ScN compared to $\text{Al}_{0.13}\text{Sc}_{0.87}\text{N}$, originates from this Drude contribution that dominates ScN's dielectric response in the long wavelength region of the spectrum. The imaginary part

of the permittivity (ϵ'') indicates high optical loss of ScN in the green part of the spectrum due to its direct interband transition, while the near IR-regions are lossy due to Drude absorption. For the $\text{Al}_x\text{Sc}_{1-x}\text{N}$ films, the peaks of ϵ'' have moved to the near-UV region corresponding to their direct energy gap, while the Drude contribution for them is negligibly small. One significant point to note is that the optical losses for the metastable rocksalt $\text{Al}_x\text{Sc}_{1-x}\text{N}$ films are higher compared to stable rocksalt or stable wurtzite phases.

5 Electrical properties To realize metal/semiconductor superlattices composed of these nitride materials, it is also very important to understand the electrical properties of $\text{Al}_x\text{Sc}_{1-x}\text{N}$. The room temperature electronic properties were measured with a 4-probe MMR Hall measurement system. The resistivity, carrier concentration, and the mobility of the as-deposited n -type ScN film are $0.1 \times 10^{-3} \Omega\text{-cm}$, $4 \times 10^{20} \text{ cm}^{-3}$, and $81 \text{ cm}^2/\text{Vs}$, respectively, and are consistent with our previous [20] results. As AlN is incorporated in the ScN matrix, the resistivity increases primarily due to the reduction in the mobility (see the inset in Fig. 3e). The carrier concentration of the rocksalt $\text{Al}_x\text{Sc}_{1-x}\text{N}$ having $0 < x < 0.52$ remains very high at $\sim 10^{20} \text{ cm}^{-3}$ due to impurities (substitutional oxygen atoms at nitrogen sites, and nitrogen vacancies). Since aluminum and scandium are iso-electronic, incorporation of AlN in ScN is not expected to reduce the carrier concentration. For films with $x = 0.62$ and 0.72 exhibiting the wurtzite phase, the carrier concentration decreases drastically to 6×10^{16} and $5 \times 10^{14} \text{ cm}^{-3}$, respectively. The resistivities of the films as a result are also very high ($90 \Omega\text{ cm}$ for $\text{Al}_{0.62}\text{Sc}_{0.38}\text{N}$, and $2 \times 10^4 \Omega\text{ cm}$ for $\text{Al}_{0.72}\text{Sc}_{0.28}\text{N}$). Because of the 20 nm TiN seed layer, we could not measure the electronic properties of the metastable rocksalt $\text{Al}_x\text{Sc}_{1-x}\text{N}$ films.

6 Conclusions In conclusion, we describe the optical and electronic properties of the epitaxial rocksalt semiconductor alloy system, $\text{Al}_x\text{Sc}_{1-x}\text{N}$. Films grown directly on (100)MgO for x up to 0.51 exhibit optical properties and XRD spectra consistent with a homogeneous single-phase rocksalt alloy. By inserting a 20 nm TiN buffer layer between the MgO substrate and the $\text{Al}_x\text{Sc}_{1-x}\text{N}$ film, the homogeneity range of the rocksalt phase can be extended to at least $x = 0.82$ for a 120 nm thick film. Within the rocksalt homogeneity range, the semiconductor exhibits a moderate direct bandgap bowing with a bowing parameter of $1.41 \pm 0.19 \text{ eV}$. The direct bandgap of metastable rocksalt-AlN is extracted to be $4.70 \pm 0.20 \text{ eV}$. The tunable lattice parameter, bandgap, dielectric permittivity, and electronic properties of $\text{Al}_x\text{Sc}_{1-x}\text{N}$ alloy enables growth of high quality epitaxial rocksalt-metal/ $\text{Al}_x\text{Sc}_{1-x}\text{N}$ superlattices with several different nitride metals (see Fig. 4), thus allowing for thermally and chemically robust engineered metamaterials based on metal/semiconductor superlattices with nanoscale periods and atomically sharp interfaces.

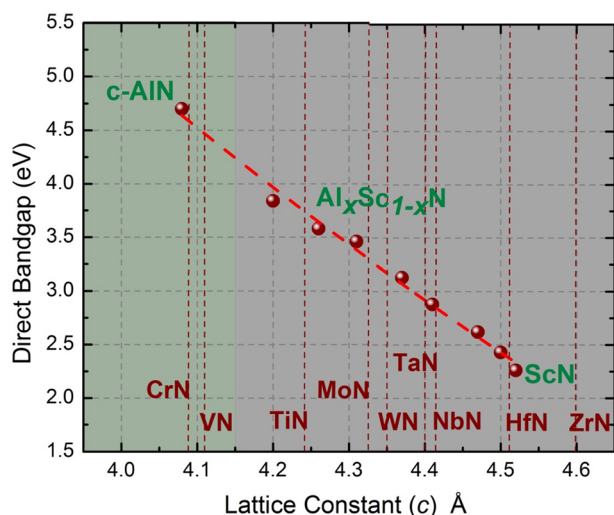


Figure 4 Phase diagram (direct bandgap vs. lattice constant) of rocksalt $\text{Al}_x\text{Sc}_{1-x}\text{N}$ thin film. Nine different transition metal nitrides are shown in the figure having lattice parameter corresponding to their horizontal axis positions. The figure suggests that rocksalt $\text{Al}_x\text{Sc}_{1-x}\text{N}$ can be used as a semiconductor component in metal/ $\text{Al}_x\text{Sc}_{1-x}\text{N}$ superlattices with all such metals and their alloys.

Acknowledgements B.S. and T.D.S. acknowledge financial support by the National Science Foundation and US Department of Energy (CBET-1048616). B.S. thanks Robert Wortman for assistance in Hall measurements. E.A.S. acknowledges support to the Center for Functional Nanomaterials, Brookhaven National Laboratory, which is supported by the U.S. Department of Energy, Office of Basic Energy Sciences, under Contract No. DE-AC02-98CH10886.

Supporting Information

Additional supporting information may be found in the online version of this article at the publisher's website.

References

- [1] S. Nakamura, *Science* **281**, 956–961 (1998).
- [2] S. Nakamura, M. Senoh, S. Nagahama, N. Iwasa, T. Yamada, T. Matsushita, H. Kiyono, and Y. Sugimoto, *Jpn. J. Appl. Phys.* **35**, L74–L76 (1996).
- [3] S. PalDey and S. C. Deevi, *Mater. Sci. Eng. A* **342**, 58–79 (2003).
- [4] T. Ikeda and H. Satoh, *Thin Solid Films* **195**, 99–110 (1991).
- [5] V. Rawat, Y. K. Koh, D. G. Cahill, and T. D. Sands, *J. Appl. Phys.* **105**, 024909 (2009).
- [6] B. N. Pantha, R. Dahal, J. Li, J. Y. Lin, H. X. Jiang, and G. Pomrenka, *Appl. Phys. Lett.* **98**, 042112 (2008).
- [7] G. V. Naik, B. Saha, J. Liu, S. Saber, E. Stach, J. Iruduraj, T. D. Sands, V. Shalae, and A. Boltasseva, *Proc. Natl. Acad. Sci.* **111**, 7546 (2014).
- [8] B. Saha, G. V. Naik, S. Saber, C. Akatay, E. Stach, V. M. Shalae, A. Boltasseva, and T. D. Sands, *Phys. Rev. B* **90**, 125420 (2014).
- [9] B. Saha, J. Acharya, T. D. Sands, and U. V. Waghmare, *J. Appl. Phys.* **107**, 033715 (2010).
- [10] M. Akiyama, T. Kamohara, K. Kano, A. Teshigahara, Y. Takeuchi, and N. Kawahara, *Adv. Mater.* **21**, 593–596 (2008).
- [11] M. Moreira, J. Bjurström, I. Katardjev, and V. Yantchev, *Vacuum* **86**, 23–26 (2011).
- [12] C. Höglund, J. Birch, B. Alling, J. Bareño, Z. Czigány, P. O. Å. Persson, G. Wingqvist, A. Zukauskaitė, and L. Hultman, *J. Appl. Phys.* **107**, 123515 (2010).
- [13] A. Zukauskaitė, G. Wingqvist, J. Palisaitis, J. Jensen, P. O. Å. Persson, R. Matloub, P. Murali, Y. Kim, J. Birch, and L. Hultman, *J. Appl. Phys.* **111**, 093527 (2012).
- [14] C. Höglund, J. Bareño, J. Birch, B. Alling, Z. Czigány, and L. Hultman, *J. Appl. Phys.* **105**, 113517 (2009).
- [15] B. Saha, T. D. Sands, and U. V. Waghmare, *J. Appl. Phys.* **109**, 083717 (2011).
- [16] B. Saha, T. D. Sands, and U. V. Waghmare, *J. Phys.: Condens. Matter* **24**, 415303 (2012).
- [17] V. Rawat and T. D. Sands, *J. Appl. Phys.* **100**, 064901 (2006).
- [18] S. Adachi, *Properties of Semiconductor Alloys: Group-IV, III–V and II–VI Semiconductors* (John Wiley & Sons, Chichester, 2009).
- [19] B. Saha, G. V. Naik, V. P. Drachev, A. Boltasseva, E. E. Marinero, and T. D. Sands, *J. Appl. Phys.* **114**, 063519 (2013).
- [20] P. V. Burmistrova, J. Maassen, T. Favaloro, B. Saha, S. Salamat, Y. R. Koh, M. S. Lundstrom, A. Shakouri, and T. D. Sands, *J. Appl. Phys.* **113**, 153704 (2013).
- [21] C. Constantin, M. B. Haider, D. Ingram, A. R. Smith, N. Sandler, K. Sun, and P. Ordejon, *J. Appl. Phys.* **98**, 123501 (2005).
- [22] F. Tasnadi, B. Alling, C. Hugland, G. Wingqvist, J. Birch, L. Hultman, and I. Abrikosov, *Phys. Rev. Lett.* **104**, 137601 (2010).
- [23] A. Madan, I. W. Kim, S. C. Cheng, P. Yashar, V. P. Dravid, and S. A. Barnett, *Phys. Rev. Lett.* **78**, 1743–1746 (1997).
- [24] R. F. C. Farrow, *J. Vac. Sci. Technol. B* **1**, 222–228 (1983).
- [25] R. Deng, S. R. Evans, and D. Gall, *Appl. Phys. Lett.* **102**, 112103 (2013).
- [26] A. Rockett, *The Materials Science of Semiconductors* (Springer, Berlin, Heidelberg, New York, 2008).
- [27] J. Wu, W. Walukiewicz, K. M. Yu, J. W. Ager III, E. E. Haller, H. Lu, and W. J. Schaff, *Appl. Phys. Lett.* **80**, 4741 (2002).
- [28] P. E. V. Camp, V. E. V. Doren, and J. T. Devreese, *Phys. Rev. B* **44**, 9096 (1991).
- [29] H. Berkok, A. Tebboune, A. Saim, and A. H. Belbachir, *Physica B* **411**, 1–6 (2013).
- [30] Z. Jiao, S. Ma, and J. Yang, *Solid State Sci.* **13**, 331–336 (2011).